

UC San Diego

UC San Diego Previously Published Works

Title

The Simons Observatory Microwave SQUID Multiplexing Detector Module Design

Permalink

<https://escholarship.org/uc/item/6tk20146>

Journal

The Astrophysical Journal, 922(1)

ISSN

0004-637X

Authors

McCarrick, Heather

Healy, Erin

Ahmed, Zeeshan

et al.

Publication Date

2021-11-01

DOI


















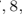







10.3847/1538-4357/ac2232

Copyright Information

This work is made available under the terms of a Creative Commons Attribution-NonCommercial License, available at <https://creativecommons.org/licenses/by-nc/4.0/>

Peer reviewed

The Simons Observatory microwave SQUID multiplexing detector module design

HEATHER MCCARRICK,¹ ERIN HEALY,¹ ZEESHAN AHMED ^{2,3} KAM ARNOLD,⁴ ZACHARY ATKINS ¹
JASON E. AUSTERMANN,⁵ TANAY BHANDARKAR ⁶ JAMES A. BEALL,⁵ SARAH MARIE BRUNO,¹ STEVE K. CHOI ^{7,8}
JAKE CONNORS,⁵ NICHOLAS F. COTHARD,⁹ KEVIN D. CROWLEY,¹ SIMON DICKER ⁶ BRADLEY DOBER ^{10,5}
CODY J. DUELL,⁷ SHANNON M. DUFF,⁵ DANIEL DUTCHER ¹ JOSEF C. FRISCH,³ NICHOLAS GALITZKI ⁴
MEGAN B. GRALLA,¹¹ JON E. GUDMUNDSSON ¹² SHAWN W. HENDERSON ^{2,3} GENE C. HILTON,⁵
SHUAY-PWU PATTY HO,¹³ ZACHARY B. HUBER ⁷ JOHANNES HUBMAYR,⁵ JEFFREY IULIANO ⁶
BRADLEY R. JOHNSON ¹⁴ ANNA M. KOFMAN ⁶ AKITO KUSAKA,^{15,16,17,18} JACK LASHNER ¹⁹
ADRIAN T. LEE ^{20,15,21} YAQIONG LI ^{7,22} MICHAEL J. LINK,⁵ TAMMY J. LUCAS,⁵ MARIUS LUNGU,¹ J.A.B. MATES,⁵
JEFFREY J. MCMAHON,^{23,24} MICHAEL D. NIEMACK ^{7,8,22} JOHN ORLOWSKI-SCHERER ⁴ JOSEPH SEIBERT ⁴
MAXIMILIANO SILVA-FEAVER ⁴ SARA M. SIMON,²⁵ SUZANNE STAGGS,¹ ARITOKI SUZUKI ¹⁵ TOMOKI TERASAKI ¹⁶
JOEL N. ULLOM,⁵ EVE M. VAVAGIAKIS,⁷ LEILA R. VALE,⁵ JEFF VAN LANEN,⁵ MICHAEL R. VISSERS,⁵ YUHAN WANG,¹
EDWARD J. WOLLACK ²⁶ ZHILEI XU ^{6,27} EDWARD YOUNG,^{2,28} CYNDIA YU,^{2,13} KAIWEN ZHENG,¹ AND NINGFENG ZHU⁶

¹Joseph Henry Laboratories of Physics, Jadwin Hall, Princeton University, Princeton, NJ 08544, USA

²Kavli Institute for Particle Astrophysics and Cosmology, Menlo Park, CA 94025, USA

³SLAC National Accelerator Laboratory, Menlo Park, CA 94025, USA

⁴Department of Physics, University of California San Diego, La Jolla, CA 92093, USA

⁵National Institute of Standards and Technology, Boulder, CO 80305, USA

⁶Department of Physics and Astronomy, University of Pennsylvania, Philadelphia, PA 19104, USA

⁷Department of Physics, Cornell University, Ithaca, NY 14853, USA

⁸Department of Astronomy, Cornell University, Ithaca, NY 14853, USA

⁹Department of Applied and Engineering Physics, Cornell University, Ithaca, NY 14853, USA

¹⁰Department of Physics, University of Colorado, Boulder, CO 80309, USA

¹¹Department of Astronomy/Steward Observatory, University of Arizona, 933 N. Cherry Ave., Tucson, AZ 85721, USA

¹²The Oskar Klein Centre, Department of Physics, Stockholm University, SE-106 91 Stockholm, Sweden

¹³Department of Physics, Stanford University, Stanford, CA 94305 USA

¹⁴Department of Astronomy, University of Virginia, Charlottesville, VA 22904, USA

¹⁵Physics Division, Lawrence Berkeley National Laboratory, Berkeley, CA 94720, USA

¹⁶Department of Physics, The University of Tokyo, Tokyo 113-0033, Japan

¹⁷Kavli Institute for the Physics and Mathematics of the Universe (WPI), Berkeley Satellite, University of California, Berkeley 94720, USA

¹⁸Research Center for the Early Universe, School of Science, The University of Tokyo, Tokyo 113-0033, Japan

¹⁹Department of Physics and Astronomy, University of Southern California, Los Angeles, CA 90089, USA

²⁰Department of Physics, University of California Berkeley, Berkeley, CA 94720, USA

²¹Radio Astronomy Lab, University of California Berkeley, Berkeley, CA 94720, USA

²²Kavli Institute at Cornell for Nanoscale Science, Cornell University, Ithaca, NY 14853, USA

²³Department of Astronomy and Astrophysics, University of Chicago, 5640 S. Ellis Ave., Chicago, IL 60637 USA

²⁴USA Kavli Institute for Cosmological Physics, University of Chicago, 5640 S. Ellis Ave., Chicago, IL 60637, USA

²⁵Fermi National Accelerator Laboratory, Batavia, IL 60510, USA

²⁶NASA Goddard Space Flight Center, Greenbelt, MD 20771, USA

²⁷MIT Kavli Institute, Massachusetts Institute of Technology, Cambridge, MA 02139, USA

²⁸Department of Physics, Stanford University, Stanford, CA 94305, USA

ABSTRACT

Advances in cosmic microwave background (CMB) science depend on increasing the number of sensitive detectors observing the sky. New instruments deploy large arrays of superconducting transition-edge sensor (TES) bolometers tiled densely into ever larger focal planes. High multiplexing factors

47 reduce the thermal loading on the cryogenic receivers and simplify their design. We present the
 48 design of focal-plane modules with an order of magnitude higher multiplexing factor than has pre-
 49 viously been achieved with TES bolometers. We focus on the novel cold readout component, which
 50 employs microwave SQUID multiplexing (μmux). Simons Observatory will use 49 modules containing
 51 60,000 bolometers to make exquisitely sensitive measurements of the CMB. We validate the focal-plane
 52 module design, presenting measurements of the readout component with and without a prototype de-
 53 tector array of 1728 polarization-sensitive bolometers coupled to feedhorns. The readout component
 54 achieves a 95% yield and a 910 multiplexing factor. The median white noise of each readout channel
 55 is $65 \text{ pA}/\sqrt{\text{Hz}}$. This impacts the projected SO mapping speed by $< 8\%$, which is less than is assumed
 56 in the sensitivity projections. The results validate the full functionality of the module. We discuss the
 57 measured performance in the context of SO science requirements, which are exceeded.

58 1. INTRODUCTION

59 The Simons Observatory (SO) is a suite of new telescopes that will be used to survey the cosmic microwave back-
 60 ground (CMB) temperature and polarization anisotropies. These observations are designed to measure or constrain
 61 the primordial B-mode polarization signal with a tensor-to-scalar ratio r uncertainty of $\sigma(r) = 0.003$, constrain the
 62 sum of the neutrino masses, and survey galaxy clusters through the thermal and kinematic Sunyaev-Zel'dovich effects,
 63 along with a number of other cosmological and astrophysical probes (The Simons Observatory Collaboration et al.
 64 2019).

65 The initial configuration of SO consists of one large 6 m aperture telescope (LAT) (Niemack 2016; Gudmundsson
 66 et al. 2021; Xu et al. 2021) and three small aperture 0.5 m telescopes (SATs) (Ali et al. 2020; Galitzki et al. 2018). The
 67 four telescopes will observe in six common spectral bands centered between **30** and 290 GHz. Collectively, dichroic
 68 pixels with over 60,000 transition-edge-sensor (TES) bolometers will be deployed to achieve the sensitivity needed for
 69 the cosmological science goals. The optical coupling, detector array, and cold readout are packaged in a universal
 70 focal-plane module (UFM). **SO will observe with 49 UFM**s. Each SAT focal plane **consists** of seven tiled UFM
 71 **The three SATs will ultimately host four focal planes over the course of the experiment, for a total of**
 72 **28 UFM**s. The LAT receiver (LATR) (Zhu et al. 2021) will contain seven optics tubes, each of which has a focal
 73 plane with three UFM, for a total of 21 UFM. The ‘universal’ name is given to the modules as they are common
 74 to all receiver focal planes. The detector arrays build on the proven detector performance of the Atacama Cosmology
 75 Telescope (ACT) (Henderson et al. 2016) and POLARBEAR (Suzuki et al. 2016) collaborations.

76 The number of detectors SO requires to meet the stated cosmological goals is a significant increase over current
 77 experiments, which in turn requires both readout and focal-plane module development. Current CMB experiments use
 78 voltage-biased TES bolometers noise-limited by photons. Their proven sensitivity across millimeter-wave frequencies
 79 makes them the standard. Thus, any significant gain in sensitivity necessarily comes from an increase in the detector
 80 count.

81 The readout architectures must advance to accommodate the growing number of TESs and associated circuitry.
 82 Simply scaling existing readout designs will result in high thermal loads, complex cryogenic wiring designs, and/or
 83 inefficient use of the focal-plane area; these are at odds with other experiment demands. For SO, we are increasing
 84 the multiplexing factor to, colloquially, 1000 (in practice, 910) in half an octave of bandwidth. This allows efficient
 85 packing of focal-plane modules and significantly decreases the cold wiring complexity as compared to current readout
 86 systems (Dobbs et al. 2012; de Korte et al. 2003), as all detectors within a module share only two transmission lines.
 87 Furthermore, we show this can be implemented in a compact assembly, which can be tessellated, enabling large, densely
 88 packed focal planes. The design is compatible with the requirement that the readout and detectors have sufficiently
 89 low noise such that the desired instrument sensitivity can be achieved.

90 1.1. Microwave SQUID multiplexing

91 SO will use microwave superconducting quantum interference device (SQUID) multiplexing (μmux) (Irwin & Lehnert
 92 2004; Mates et al. 2008) to read out the detectors. Microwave SQUID multiplexing transforms a change in TES current
 93 into a shift in resonance frequency f_0 of a resonator, which is read out through a phase shift of the interrogating probe
 94 tone. A schematic is shown in Fig. 1. Each TES is inductively coupled to a radio frequency (RF) SQUID, which is in
 95 turn inductively coupled to a quarter-wave co-planar CPW resonator. Each resonator has a different electrical length

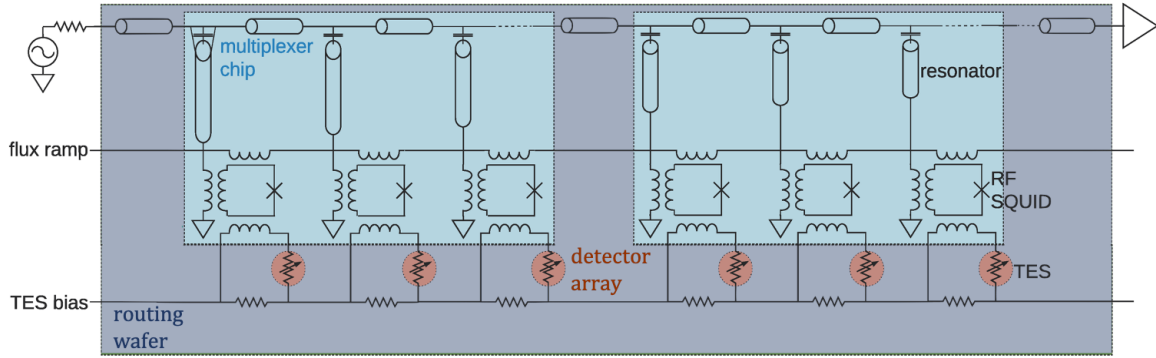


Figure 1. Schematic showing the microwave SQUID multiplexing (μmux) circuit and implementation in the Simons Observatory focal-plane module. The routing wafer is marked in *grey*, multiplexer chips *blue*, and TES detector array *red*. See [Mates \(2011\)](#) for additional details of the on-chip μmux circuit.

and thus unique f_0 , allowing many channels to be read out on a single transmission line. The flux ramp is a second input to the SQUID; it continually applies a sawtooth signal, which linearizes the SQUID response and modulates (at ~ 16 kHz) the TES signal above any elevated $1/f$ noise, including the two-level system noise frequently seen in microwave resonators ([Gao et al. 2008](#)). Microwave multiplexing is a novel readout method for CMB experiments and offers an elegant solution for multiplexing an order of magnitude more detectors than previous architectures.

In the remainder of this paper, we detail and motivate the design of the readout module in [Sec. 2](#), validate the design in [Sec. 3](#), discuss the performance in the context of SO requirements in [Sec. 4](#), and conclude with possible future directions in [Sec. 5](#).

2. DESIGN

2.1. Readout overview

The SO readout system consists of three parts: the warm electronics, the readout wiring (RF chains and DC wiring), and the cold (100 mK) multiplexer assembly, the last of which this paper details. For the warm readout (300 K and external to the cryostat), SO uses the SLAC Superconducting Microresonator Radio Frequency (SMuRF) electronics ([Henderson et al. 2018](#)). SMuRF generates the tones which drive, interrogate, and track the resonators and provides the DC TES biases and flux ramp signals (nominally 4 kHz). The probe tones enter and exit the cryostat via the RF chains. The RF chains ([Sathyanarayana Rao et al. 2020](#)) contain a series of attenuators on the input side to achieve the desired tone power at the cold multiplexer input. Two-stage amplification (at 4 K and 40 K) on the output, in concert with the tone tracking, achieves high gain with sufficient linearity to maintain low noise at the total power needed for 910 tones.

2.2. Readout module

The novel part of the UFM is contained in the readout module, referred to as the universal μmux module (UMM). The UMM is a compact, low-profile assembly that sits directly behind the 150 mm diameter detector array, occupying the same footprint. The UMM is shown in [Fig. 2](#) and the comprising detector and μmux components are given in [Table 1](#). Two pairs of coaxial lines read out the detectors for a total of 1820 channels in a 2×910 configuration. Twenty-eight multiplexer chips (2×14) read out between 4–6 GHz are mounted to a monolithic copper piece that provides both a ground plane and mechanical support. The microwave readout and flux ramp circuits continue on a monolithic silicon routing wafer mounted in the same plane as the multiplexer chips. The routing wafer also provides the $400 \mu\Omega$ shunt resistors for each TES bias circuit, and the routing for twelve TES bias lines. The shunt resistances were chosen to be 10% of the TES operating resistance while the bias line number was informed by the achieved uniformity of the Advanced ACTPol arrays. Each detector array contains up to 1728 optically coupled detectors (and 36 dark bolometers). The UFM is operated at a bath temperature of 100 mK. We discuss the components and design choices in more detail in the remainder of this section, and touch on the assembly process ([Healy et al. 2020](#)), which is an important component in achieving good RF performance.

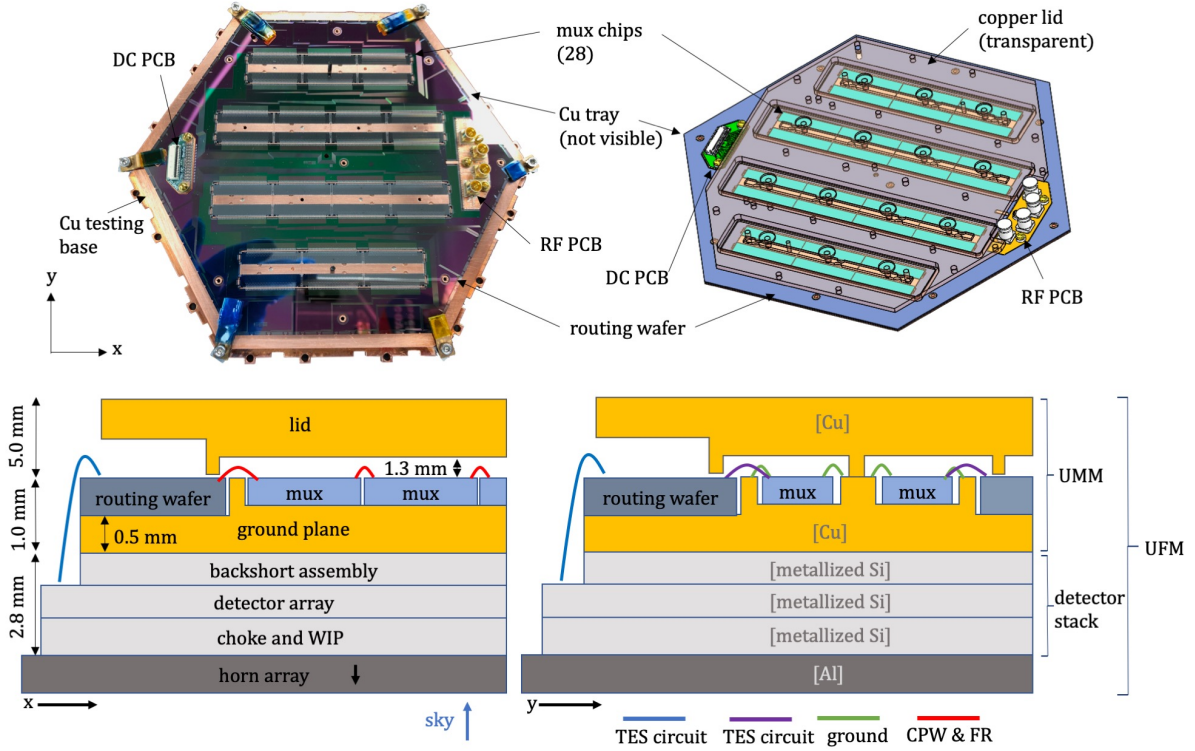


Figure 2. *Upper* Photograph and rendering of the readout module, which contains the 100 mK readout components. The lid is removed to reveal the silicon components, including the two sets of 14 multiplexer chips, containing the 1820 readout channels, and the routing wafer, which connects the multiplexer chips in series and hosts the TES bias circuitry. The silicon components rest on a copper plane, which is the RF ground and mechanical support. The μ mux components are independently characterized before being coupled to a detector array. The right rendering shows the copper lid (transparent). *Lower* Cross-sectional views (not-to-scale) of the universal focal-plane module. The left view illustrates that rows of multiplexer chips are connected in series at the coplanar waveguide (CPW) and flux ramp with wirebonds, as shown in *red*. The right shows a portion of the ground bonds that are made between the multiplexer chips and ground plane as well as the enclosure of the multiplexer chips into cavities. In both views, the electrical connections of the transition-edge sensor (TES) circuit, are achieved through wirebonds. This connection between multiplexer chip and routing wafer is denoted in *purple* and between the routing wafer and detector array in *blue*. The approximate z -dimensions are shown in millimeters.

129 A single multiplexer chip contains 66 multiplexer channels, one of which is used for noise diagnostics and one of
 130 which terminates at a bare resonator. Briefly, each channel on the chip consists of TES inputs, an RF SQUID, and
 131 a quarter-wave resonator with a unique f_0 set by the CPW length. The resonators are capacitively coupled to a
 132 common CPW transmission line. The common flux ramp line is inductively coupled to the SQUIDS. The resonators
 133 are designed to have a bandwidth $b_r = 100$ kHz, which is achieved by tuning the coupling quality factor Q_c for a given
 134 f_0 and internal quality factor Q_i . The coupling here refers to that between the resonator and transmission line. A set
 135 of 14 multiplexer chips covers the 4–6 GHz readout bandwidth (Dober et al. 2021).

136 A copper plane physically hosts the multiplexer chips and provides a ground reference for the UMM. This copper
 137 plane is $500 \mu\text{m}$ thick and machined into a hexagon of the same dimensions as the routing wafer. The multiplexer
 138 chips are diebonded with rubber cement onto the copper plane using a flip chip bonder. Extruded features surround
 139 rows of either three or four multiplexer chips. These features are paired to those in a copper lid, which mates to the
 140 copper plane. This effectively reduces the size of the RF package to reduce the number and coupling to low-frequency
 141 box modes, which have been observed to degrade the resonator Q_i and thus performance. The lid hosts pogo-pins,
 142 which push down on and mechanically restrain the routing wafer.

143 The copper plane also critically acts as the RF ground and is continuous beneath the multiplexer chips. Early
 144 versions used a silicon wafer with a monolithic, deposited ground plane, which compromised the achievable resonator
 145 quality factor and motivated the use of a copper ground plane (J.A.B. Mates 2019, private communications). Due to
 146 the segmented nature of the assembly – with 28 multiplexer chips – it is crucial that all of the ground planes be tied

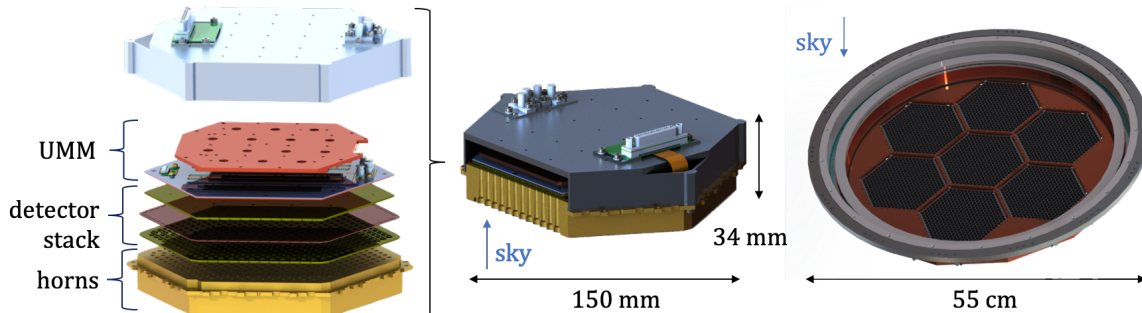


Figure 3. *Left* Exploded view of the SO focal-plane module. The UFM is comprised of (i) the UMM *blue and copper*, (ii) the detector stack *yellow* including the array *pink*, and (iii) the horns *gold*. After validation, the UMM is transferred on top of the detector wafer stack. The TES bias line connections between the routing wafer and detector array are made with wirebonds around the perimeters. *Center* Assembled view of the SO UFM. Not pictured is an outer aluminum shield nor the corresponding connectors to the receiver wiring. *Right* Rendering of the first SAT focal plane with seven detector arrays. Tightly packing the hexagonal detector tiles in the SAT focal planes limits how large the readout module area can be while the LAT focal planes (not shown) limit the height.

147 together with a sufficiently low RF impedance. The resonator Q_i is sensitive to the nearby grounding scheme. The
 148 modularity of the multiplexer chips allows for ground connections to the copper plane via wirebonds at each chip very
 149 close to each resonator. The grounds of the multiplexer chips and the routing wafer are tied together with wirebonds
 150 as well. The connection from the RF ground to the package is made via a PCB; the PCB is connected to the package
 151 ground with vias and the routing wafer ground with wirebonds. This PCB transitions the RF signal and ground to the
 152 plane of the silicon components via a CPW to surface mount sub miniature push-on (SMP) transition. The RF signals
 153 ultimately interface to the receiver wiring through conventional feedthroughs, which mate to the SMP connectors.
 154 This architecture effectively brings all necessary electrical lines into the module without using focal plane area.

155 The lithographed routing wafer serves the dual purpose of (i) connecting the rows of multiplexer chips in series and
 156 (ii) providing the TES bias circuitry. First, the routing wafer has cutouts at the multiplexer chip locations, and thus
 157 fits around the rows of multiplexer chips like a frame and rests on the copper plane. The silicon is 500 μm thick and
 158 etched into a hexagonal shape from a 150 mm diameter wafer. Superconducting CPW and flux ramp lines are routed
 159 between the multiplexer chip rows on the wafer. Wirebonds connect the flux ramp and CPW lines on the multiplexer
 160 chips and routing wafer in series with 18 interconnections for each of the sets of 14 multiplexer chips. The CPW
 161 wirebonds are made such that the impedance mismatch ($< 5 \Omega$) due to the wirebond inductance is minimized (Li
 162 et al. 2020); a full schedule is shown in Healy et al. (2020). The routing wafer also connects the transmission lines
 163 of the first and last multiplexer chips to the RF and DC boards that interface with the rest of the cryostat. Second,
 164 the routing wafer hosts the TES shunt resistors and bias lines. The TES inputs are wirebonded from the multiplexer
 165 chips to the routing wafer. The bias lines emerge at bond pads at the perimeter of the routing wafer. The TES bias
 166 signals interface to the routing wafer via the planar DC PCB board, which is also the launch point for the flux ramp
 167 signals. These signals ultimately interface with the receiver wiring through a flex-cable, which ends in a conventional
 168 connector (a Micro D-subminiature).

169 2.3. Focal-plane module

170 An exploded view of the UFM is shown in Fig. 3. The UFM is comprised of three parts: the UMM, the detector
 171 stack, and the optical coupling. Each SO detector array will have 1764 bolometers (Hill et al. 2018) for both the
 172 mid-frequencies (MF) (90, 150 GHz) and ultra-high frequencies (UHF) (220, 290 GHz) (Walker et al. 2020; Stevens
 173 et al. 2020), arranged in a hex-pack at a 5.3 mm pixel pitch. The low frequencies (LF) (30, 40 GHz) will have fewer
 174 detectors. The MF and UHF use arrays that detect photons via horn-coupled ortho-mode transducers (Simon et al.
 175 2018), while the LF uses lenslet-coupled sinuous antennas (Suzuki et al. 2012).

176 The UFM design - except for the detector parameters and horn profile - is identical across MF and UHF frequency
 177 bands and receivers. Thus, the UFM design must comply with constraints from both the SATs and LATR. The efficient

Table 1. Focal-plane module components are given below for clarity. Each UFM has two halves, fed by a pair of coaxial cables. The LF focal-plane module has fewer detectors and will use a simplified version of the readout assembly.

| Component in UMM/UFM | Quantity per coaxial chain | Quantity per module |
|-------------------------------|----------------------------|---------------------|
| Multiplexing chips | 14 | 28 |
| Multiplexing channels | 910 | 1820 |
| Optical detectors | 864 | 1728 |
| Dark detectors | 12 (or 24) | 36 |
| Transmission lines | 1 | 2 |
| Flux ramp lines | 1 | 2 |
| TES bias lines | 6 | 12 |
| Component in multiplexer chip | | Quantity |
| Channels | 64 | |
| Diagnostic channels | 2 | |

filling of the focal plane for the SAT, with seven tessellated UFM, motivates the development of the cold readout to only occupy the same footprint as the detector arrays. The tight space constraints in the LATR optics tubes dictates the maximum height of the UFM.

In the UFM, the UMM is vertically placed atop the detector stack, which itself is already paired to the primary optical coupling both mechanically and thermally, the latter via gold wirebonds. The components are aligned via a central and an outer dowel pin, which are terminated in the optical coupling (i.e. horns). The detector stack and UMM each have a central pin hole and outer slotted hole. The latter is sized to accommodate the difference in thermal contractions between components when the modules are cooled to the 100 mK operating temperature.

The optical coupling has a mechanical flange that interfaces to the receiver, wherein the focal-plane modules are tiled. The TES bias connections along the perimeter of the UMM are wirebonded to the detector wafer, completing the electrical circuits within the module. The assembly is enclosed by a superconducting aluminum outer shield, which also provides force on the readout and detector stack through integrated tripods, completing the mechanical packaging. The aforementioned DC and RF connectors that interface to the cryostat are fed-through and attached to this outer shield.

3. DESIGN VALIDATION

To validate the design, we assess the performance of the readout and focal plane modules. The UMM implements the highest TES multiplexing factor to date. Demonstrating its functionality also validates the full system: the complete complement of multiplexer chips, the RF chain and the warm electronics, SMuRF. We first test the multiplexing module in isolation (no TESs), and second when connected to optically coupled TESs. We report measurements of the yield, noise properties, and RF transmission of the multiplexing module in Sec. 3.1. We then look at the performance when connected to a detector array, reporting the yield, noise properties and detector saturation powers in Sec. 3.2. The performance exceeds the science requirements in all cases, as discussed in Sec. 4.

3.1. Readout module

We characterize the multiplexing module in isolation to assess its performance and validate the design choices. In this configuration, the UMM is simply mounted to a copper base in lieu of the detector stack and enclosed by the aforementioned aluminum shield. The shield will remain in place for the UFM configuration. The UMM is as described in the design section with an exception: one multiplexer chip was replaced by a through CPW. The testbed is schematically depicted in Fig. 4. Critically, the two-stage amplification RF chain discussed previously is implemented in the dilution refrigerator. The UMMs are cooled to 100 mK.

The first performance diagnostic is to quantify the RF transmission. We measure the forward scattering parameter S_{21} (and S_{43}) through the assembly with a standard vector network analyzer. Representative scattering parameter

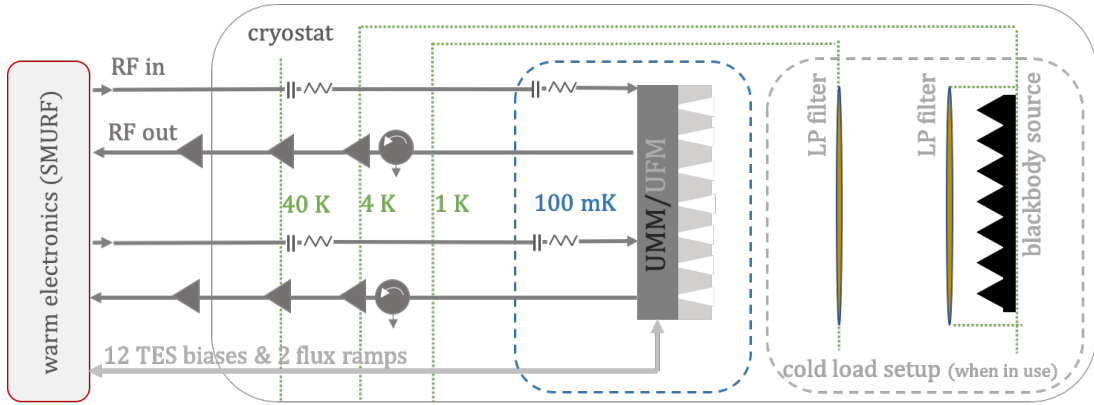


Figure 4. Schematic showing the cryogenic readout system and optical testing setup used for design validation. The readout consists of the warm electronics, called SMuRF (Henderson et al. 2018), the RF chain, and the cold multiplexer module. The warm readout generates and reads back the RF probe tones, low-frequency flux ramp signals, and TES bias pairs; the RF chain brings the signal to and from the UMM, the cold multiplexer. The two-stage low-noise cold amplification achieves high gain while providing sufficient linearity to drive the 2×910 resonators. Optical testing of the UFM uses a blackbody cold load shown at right.

209 are shown in Fig. 5. We find 1728 resonators, including diagnostic channels, or that 97% of the resonators yielded.
 210 We fit a complex model (Khalil et al. 2012) to the transmission data in order to extract the resonator parameters.
 211 This yields the complex resonator coupling quality factor Q_c and total resonator quality factor Q_r . We define Q_i as
 212 $Q_i^{-1} = Q_r^{-1} - \text{Re}(Q_c)^{-1}$; thus Q_i includes all sources of loss. The median Q_i is $\sim 7 \times 10^4$. The corresponding median
 213 resonance depth is 6.4 dB; this is defined as the difference between the local baseline off-resonance transmission and
 214 the resonance minimum. The median resonator bandwidth b_r is ~ 80 kHz. The scattering parameters for inter-line
 215 isolation are S_{23} (and S_{41}), but we compare these levels to the transmission S_{21} (and S_{43}) level to account for the
 216 losses between the calibration referenced plane and the device. We find that this exceeds 20 dB at all but the highest
 217 frequencies.

218 Second, we measure the noise. With the SMuRF warm electronics, both sides of the UMM are multiplexed, meaning
 219 all the channels on both halves are read out simultaneously for a multiplexing factor of 2×910 . The optimized drive
 220 power per resonator at the UMM input is approximately -78 dBm. The noise is measured by taking time-ordered data.
 221 The noise properties are measured by computing the amplitude spectral density for each readout channel from the
 222 corresponding time-ordered data and fitting a noise model. The model is parameterized by a low-frequency knee f_k^α ,
 223 where α is a free index, and the white noise level w_1 . The high-frequency roll-off is determined by the anti-aliasing
 224 filter. The median input-current-referred white noise level or noise-equivalent-current (NEI), as fit from this model, of
 225 the 1608 μmux channels is $65 \text{ pA}/\sqrt{\text{Hz}}$ (as shown in Fig. 5), with a median f_k of < 0.02 Hz. The noise is much smaller
 226 than the expected on-sky TES-current noise, which, for SO, is $160 \text{ pA}/\sqrt{\text{Hz}}$ in the 90 and 150 GHz spectral bands.

227 The final key performance criteria is the yield. On the UMM half with a full complement (14) of multiplexer chips
 228 and 910 readout channels, the yield is 95%. We find a 92% total yield with 1608 channels across the full module as
 229 reported in the plots in Fig. 5. The 8% loss can be attributed to the minority of resonators that had collisions in
 230 frequency space, fell outside the SMuRF-defined band filters, or were coupled to a SQUID with an anomalous response.

231 We configure a separate readout module specifically to measure crosstalk between the two halves. As previously
 232 described, the resonator frequencies are repeated twice in each readout module, once on each half. We thus are
 233 concerned with measuring the crosstalk between resonators that fall very close to one another in frequency space
 234 across the two halves. The crosstalk within an individual multiplexer chip, measured with a ‘victim and perpetrator’
 235 set-up, was shown to be $< 0.3\%$ (Dober et al. 2021). Using the same method with the UMM, we choose a ‘perpetrator’
 236 resonator with the ‘victim’ resonators on the other half of the array. The closest resonance frequencies across the two
 237 halves fall within one linewidth (< 100 kHz) of each other. We measure the maximum crosstalk between the channels
 238 to be $< 0.1\%$.

239 3.2. Focal-plane module

240 We characterize the UFM to demonstrate the readout module’s integrated performance and validate the overall
 241 design. The readout module is coupled to a MF prototype SO detector array and horn array. We characterize the

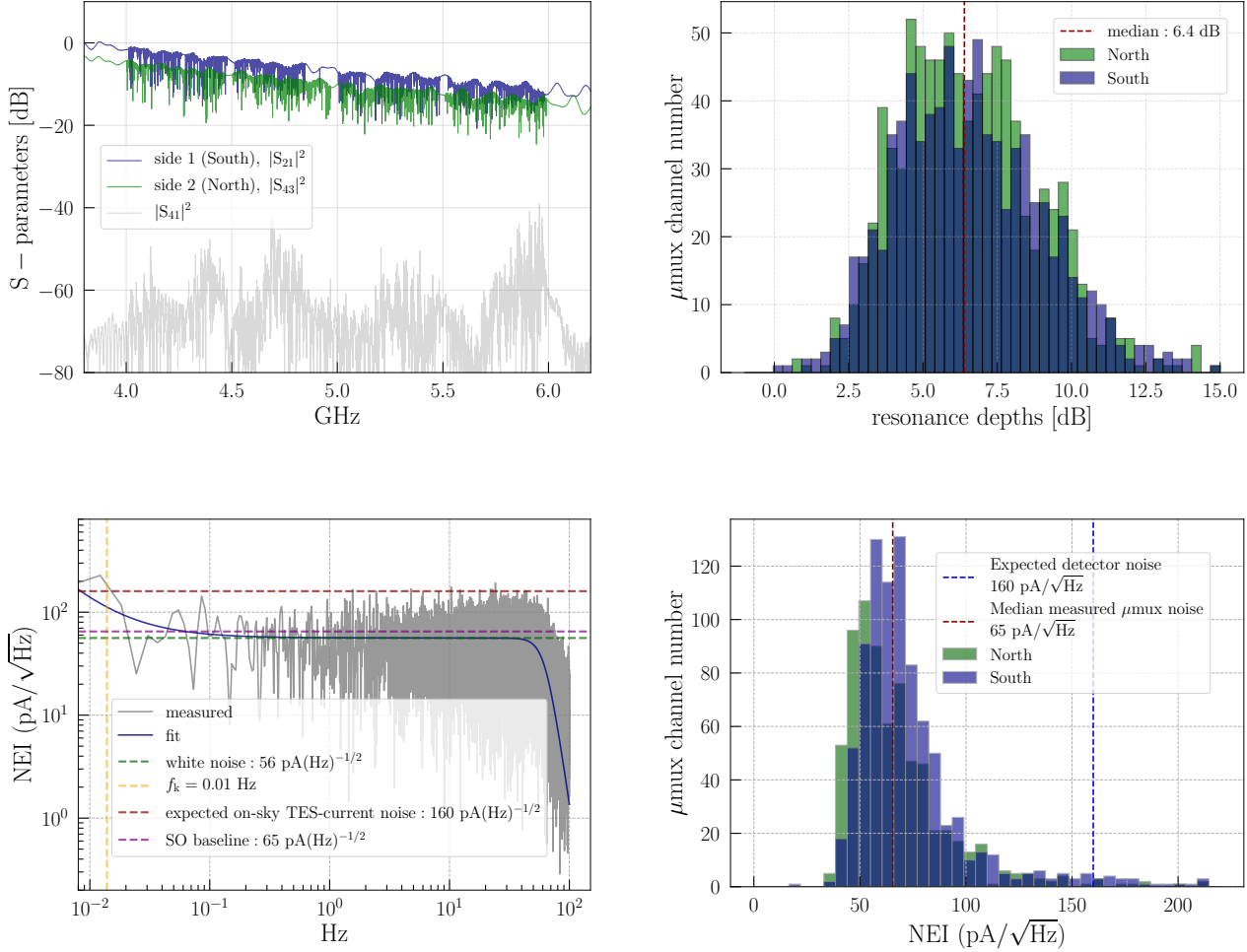


Figure 5. *Upper left* Transmission through the two sides of a prototype universal μ mux module (UMM), each spanning 4–6 GHz. The two halves are referred to as North and South. The isolation between the UMM halves is shown in *grey*. The reference plane is at the 300 K shell of the cryostat. The number of readout channels yielded is 1608 for a 92% yield. *Upper right* Histogram of the resonance depths. *Lower left* Noise spectrum of a typical multiplexer channel. Here, the white noise level S_w (green) is $56 \text{ pA}/\sqrt{\text{Hz}}$ and the upper bound of the frequency knee f_k is 0.01 Hz. The SO baseline requirement (purple) is an f_k of 0.1 Hz with $S_w < 65 \text{ pA}/\sqrt{\text{Hz}}$. The expected on-sky TES-current noise (red) is approximately $160 \text{ pA}/\sqrt{\text{Hz}}$ in the 90 and 150 GHz spectral bands. *Lower right* Histogram of the white noise levels of the cold multiplexer, without TESs attached. The array NEI meets the sensitivity necessary to reach the baseline SO forecast (The Simons Observatory Collaboration et al. 2019).

242 UFM in laboratory in two separate configurations: (i) the horn apertures are covered at 100 mK and (ii) the horn
 243 apertures are exposed to an 8.5 K blackbody load. In the second configuration, the spectral band is defined by 1 K
 244 and 4 K low-pass filters and the on-chip frequency filters fed by the high-pass cylindrical waveguide, which is the input
 245 guide.

246 First, we re-evaluate aspects of the readout now that it is coupled to a detector array. Significantly, we see no
 247 degradation of Q_i and thus expect the readout noise to remain the same as when measured independently. The
 248 resonator yield also remains unchanged.

249 Second, we measure the saturation power P_{sat} of the TES bolometers in the dark configuration, with the horn
 250 apertures covered at 100 mK. To do this, the TES biases are stepped over a range in which the detectors are taken
 251 from normal to superconducting and the current is measured at each step, mapping out an IV curve. The resulting
 252 detector saturation powers, defined at 90% of the normal resistance, are shown in Fig. 6. The median saturation

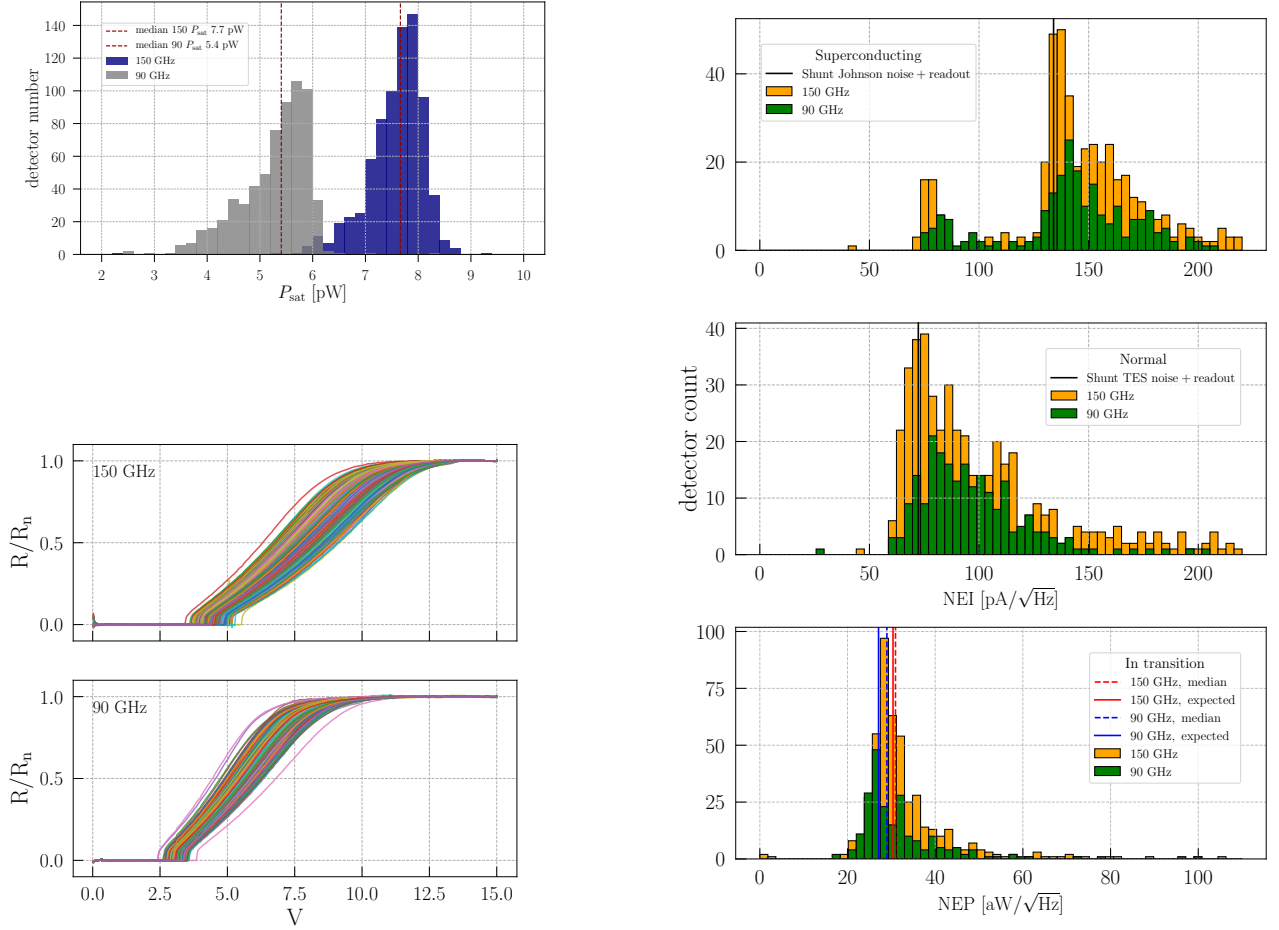


Figure 6. *Upper left* The saturation powers P_{sat} for the detectors sensitive to 90 and 150 GHz are shown in grey and blue, respectively. The median P_{sat} for the 90 and 150 GHz detectors are 5.2 and 7.3 pW. The array operability yield is 82%. *Lower left* The normalized resistances of the TESs sensitive to 90 and 150 GHz as they are biased through transition. Each line represents a different detector; the uniformity of the detectors is evident as is the large range over which they can be biased. *Right* Histograms of the white noise level of the UFM detectors as measured with the 910 multiplexer; the TESs are in the superconducting, normal, and in-transition states and exposed to an 8.5 K blackbody. The dashed vertical lines show the measured median noise per spectral band and the continuous vertical lines, the expected median noise including the photon noise from the blackbody loading. For both the 150 and 90 GHz detectors, the noise is within 10% of expectation. Note that (i) the low population in the superconducting histogram is due to the uncoupled readout channels and (ii) the x-axes are in reported in NEI for the top two histograms and in NEP for the bottom. See Appendix A for details on the expected noise.

253 powers for the 90 and 150 GHz detectors are 5.2 and 7.3 pW, within 0.2 pW of the SO target for these prototype
 254 arrays. The on-specification P_{sat} measurements indicate no significant heating on the detector array, which would tend
 255 to reduce the observed saturation power. The operable yield in the UFM is 82%.

256 Third, we measure the noise with the TES bolometers in the normal, superconducting and in-transition states with
 257 the horn aperture exposed to the 8.5 K blackbody load. The histograms in Fig. 6 show the measured and expected
 258 white noise levels in the three states. In the superconducting, the measured median is $143 \text{ pA}/\sqrt{\text{Hz}}$. The Johnson noise
 259 from the shunt resistors, which are measured directly on the routing wafer to be $400 \mu\Omega$ during screening, is added in
 260 quadrature to the previously measured readout noise (as in Sec. 3.1) to find the total expected noise of $134 \text{ pA}/\sqrt{\text{Hz}}$;
 261 the noise is within 7% of expectation. With the TES bolometers in the normal state, the measured noise is similarly in
 262 agreement with expected noise. The in-transition noise is within 10% of the expected noise (detailed in Appendix A)
 263 for both the 90 and 150 GHz detectors.

4. SIMONS OBSERVATORY REQUIREMENTS AND CONTEXT

The science case and forecast for SO is presented in [The Simons Observatory Collaboration et al. \(2019\)](#). The primary forecast is referred to as ‘baseline’. A secondary, more aggressive forecast is referred to as ‘goal’, **and is discussed in the subsequent section**. We assess whether the UFM performance meets the baseline metrics, which requires that (i) the readout reduce the observatory mapping speed by less than 18%, (ii) the readout have a low-frequency knee less than 0.1 Hz and (iii) the module have an end-to-end yield is $> 70\%$. As will be shown in this section, the **baseline** requirements are met.

First, we assess the readout measured independently. The noise due to the readout at full multiplexing will only result in an 8% degradation of total detector noise. This is better than the target level of 10% needed to achieve the baseline SO sensitivity. The yield exceeds the 78% readout yield required for SO. Thus, the weighted readout array NEI is better than required. The measured low-frequency knee, is constrained to below 0.03 Hz, better than the 0.1 Hz requirement. These noise measurements also demonstrate that the nonlinearity of the end-to-end readout system is sufficient such that the third-order intermodulation products are small enough not to cause an excess of noise at the full multiplexing factor.

Second, we assess the UFM performance given the desired SO science goals. The in-transition noise for the 90 and 150 GHz detectors are below the increased 30% noise budget allocated in the forecasting. The 82% end-to-end yield exceeds the baseline requirements. In essence, the focal-plane module design is fully functional and exceeds the requirements necessary to meet the science goals.

The readout modules presented in this paper will be used with both the MF and UHF detector arrays, comprising the MF and UHF UFM. The LF modules, with < 200 detectors per array, will use a simplified readout module design of the same footprint. The first UFM will be deployed within a year. There will be a total of 49 UFM across the four receivers. There are four focal planes for the three SATs (two MF, one UHF, and one LF); the three higher frequency focal planes will deploy initially. The LATR ([Xu et al. 2020](#)) will host seven optics tubes (**four MF, two UHF, and one LF**), each of which has a focal plane with three UFM, for 21 UFM in total. The LATR has been designed to hold 13 optics tubes and can host up to 39 UFM.

5. FUTURE OUTLOOK

This focal-plane module design has successfully placed 1820 readout channels in a 150 mm diameter assembly with noise subdominant to the expected on-sky detector noise. The performance is better than the SO requirements. This paper shows the feasibility of using μ mux in large-scale experiments. Until now, μ mux has been in development and deployed on smaller scales as an individual module ([Dicker et al. 2014](#)) or technology demonstration [Cukierman et al. \(2020\)](#); the results presented here demonstrate the feasibility of employing the technology to unlock large-scale instruments. The focal-plane modules offer an elegant and now proven design not only for SO but also other receivers, many of which are planned for the imminent future ([The CMB-S4 Collaboration et al. 2020](#); [Terry et al. 2019](#)). The high-performance design of next-generation, large-scale arrays is a critical area of study not only for millimeter-wave astrophysics but also necessarily for a larger science landscape from x-ray experiments ([Yoon et al. 2018](#)) to quantum computing ([Rosenberg et al. 2019](#)).

While stressing that the readout system already meets the baseline requirements for SO to achieve the planned science, we can also place the current tests relative to the ‘goal’ performance requirements. We could plan to improve the readout system along three axes. First, we aim to improve the yield, by making incremental changes to the module design and multiplexer chips, such as addressing small shifts in absolute frequency placement. Second, we aim to reduce the per-channel readout noise to be consistently below $< 45 \text{ pA}/\sqrt{\text{Hz}}$. This performance has been demonstrated in preliminary UMMs. The data presented in this paper, which meets baseline requirements, is shown due to the comprehensive end-to-end testing, including in the UFM configuration. This requirement has also been consistently met in the NIST μ mux assemblies with multiplexing factors of 512 ([Henderson et al. 2018](#); [Dober et al. 2017](#)) but in packaging that cannot be coupled to on-sky detectors. The multiplexer chips measured individually and in the aforementioned packaging achieve higher in-situ Q_i . The difference in achieved performance can be attributed to a combination of factors including the packaging-loss due to the overall dimensions. However, we repeat that the Q_i measured in the current UMM design are sufficient for the SO noise requirements. We also expect there are incremental gains which can be made by further optimizing SMuRF for the UFM. Finally, we are looking at increasing the multiplexing factor of the current module to 1820 and read out each module with a single pair of coaxial cables (instead of two), further decreasing wiring complexity and thermal loading in the receivers. The overall design of the

UFM is compatible with an 1820 multiplexer using 1×28 multiplexer chips to cover a 4–8 GHz bandwidth. Both the multiplexer chips and SMuRF have demonstrated their respective capabilities in the 6–8 GHz range.

To conclude, we have presented the design choices and in-lab demonstrations that validate this overall focal-plane architecture. We demonstrated the 910 multiplexer with a 95% yield in the focal-plane packaging. Multiplexing all channels, the median white noise is $< 65 \text{ pA}/\sqrt{\text{Hz}}$, only a 8% decrease in sensitivity compared to the expected on-sky TES noise, with the largest number of channels multiplexed to this date. With the UMM, we have demonstrated the operation of a SO TES bolometer array within the focal-plane module, the UFM. The first UFM's are to be integrated into the SO receivers within the next year.

This work was supported by a grant from the Simons Foundation (Award #457687, B.K.). SKC acknowledges support from NSF award AST-2001866. YL acknowledges Kavli Institute at Cornell Postdoctoral Fellowship. This document was prepared by the Simons Observatory using the resources of the Fermi National Accelerator Laboratory (Fermilab), a U.S. Department of Energy, Office of Science, HEP User Facility. Fermilab is managed by Fermi Research Alliance, LLC (FRA), acting under Contract No. DE-AC02-07CH11359. ZX is supported by the Gordon and Betty Moore Foundation.

APPENDIX

A. EXPECTED NOISE

In this appendix, we present the calculation for the expected noise of the readout and detectors, which is referenced in Sec. 3.2 and Fig. 6. The expected noise is calculated for the TES bolometers in three states: superconducting, normal, and in transition.

We consider contributions from the readout noise (ro); Johnson noise in the shunt resistance (J,s); Johnson noise in the TES when it is normal (J,n); thermal carrier noise in the TES bolometers (G); and bolometer noise due to photon loading (γ). The parenthetical labels are used as subscripts below. The μmux readout architecture converts power fluctuations at each TES bolometer into current fluctuations, which inductively induce changes in the resonator frequency. Ultimately, the signal is read out in radians and referenced to current through the TES, proportional to the mutual inductance between the SQUID and resonator. The first three noise terms listed above arise as current noise (NEI) but can be converted to power units (NEP) by noting that in the TES, power fluctuations δP are related to current fluctuations δI by the voltage across the TES, V_{TES} : $\delta P = \delta I V_{\text{TES}}$. Thus,

$$\text{NEP} = V_{\text{TES}} \text{NEI}.$$

In practice, we use $V_{\text{TES}} = (I_{\text{bias}} - I_{\text{TES}})R_{\text{sh}}$, where I_{bias} is calculated from the warm, commanded voltage and known wiring resistance leading to the array, I_{TES} is measured as described above, and R_{sh} is the shunt resistance, designed and measured to be $400 \mu\Omega$ in screening.

The expected total noise in the three scenarios is:

1. Superconducting: $\text{NEI}_{\text{s}} = (\text{NEI}_{\text{ro}}^2 + \text{NEI}_{\text{J,s}}^2)^{(1/2)}$,
2. Normal: $\text{NEI}_{\text{n}} = (\text{NEI}_{\text{ro}}^2 + \text{NEI}_{\text{J,n}}^2)^{(1/2)}$,
3. In transition: $\text{NEP}_{\text{t}} = (\text{NEP}_{\text{ro}}^2 + \text{NEP}_{\text{G}}^2 + \text{NEP}_{\gamma}^2)^{(1/2)}$.

A.1. Current noise

The readout noise is measured directly in the UMM configuration (no TESes). This level is used as our expected readout noise when calculating the expected total noise in the UFM configuration. The Johnson noise when the TES is superconducting is due entirely to the shunt resistor and is given as

$$\text{NEI}_{\text{J,sh}}^2 = \frac{4k_{\text{B}}T_{\text{b}}}{R_{\text{sh}}},$$

where k_B is the Boltzmann constant and T_b the array bath temperature, at which the shunt resistors are held. When the TES is normal, with resistance R_n , the Johnson noise is given as

$$\text{NEI}_{\text{J, TES}}^2 = \frac{4k_B T_c}{R_n},$$

where T_c is the TES critical temperature. The contribution from the shunt is negligible as $R_n \gg R_{\text{sh}}$. The normal resistance is designed to be 8 m Ω ; actual values are extracted from the IV curve measurements.

A.2. TES thermal carrier noise

With the TES in transition, the bolometer thermal carrier noise is (Mather 1982):

$$\text{NEP}_G^2 = 4k_B F T_c^2 G s_i,$$

where G is the bolometer thermal conductance, s_i is the responsivity, and F is a numerical factor related to the thermal conduction index n . We estimate the noise with $F = 1$. The factors of G and T_c are extracted from fitting data taken from T_b sweeps: an IV curve is taken as T_b is stepped from well below to above T_c and the P_{sat} measured at each step. The P_{sat} as a function of T_b is fit to the typical relation (Irwin & Hilton 2005) $\kappa(T_c^n - T_b^n)$, where κ is a constant, which directly yields T_c and n . G can then be calculated as $G = n\kappa T_c^{n-1}$. The responsivity is calculated from the local slope from the IV curve (Irwin & Hilton 2005).

A.3. Photon noise

In transition, the photon noise is the dominant noise source. The photon noise is calculated as (Zmuidzinas 2003)

$$\text{NEP}_p^2 = 2 \int_{\nu_{\text{lp}}}^{\nu_{\text{hp}}} \left[h\nu p(\nu) B(\nu) + (p(\nu) B(\nu))^2 \right] d\nu.$$

Here, ν is the photon frequency, which for these paper measurements, is emitted by the cold blackbody ($T = 8\text{--}20$ K), and ν_{lp} and ν_{hp} are the frequencies over which the expression is integrated and outside the expected bandpass. The power spectral density $p(\nu)$ can be further expanded as $p(\nu) = S(T, \nu) \eta \epsilon(\nu)$, in which $S(T, \nu)$ is the standard modified blackbody equation for a single polarization and single mode at temperature T , $\epsilon(\nu)$ is the emissivity (in practice, taken to be 1), and η is the detector optical efficiency, gathered by measuring P_{sat} as a function of stepped T (as in Choi et al. (2018)) with a prototype detector array of the same design and fabrication run. $B(\nu)$ is the cumulative bandpass, which has multiplicative contributions from the band defining elements: the metal-mesh filters (the spectra are measured separately), low-pass waveguide (simulated), on-chip frequencies filters (simulated) and beam-fill fraction (calculated).

REFERENCES

- Ali, A. M., Adachi, S., Arnold, K., et al. 2020, Journal of Low Temperature Physics, 200, 461, doi: [10.1007/s10909-020-02430-5](https://doi.org/10.1007/s10909-020-02430-5)
- Choi, S. K., Austermann, J., Beall, J. A., et al. 2018, Journal of Low Temperature Physics, 193, 267, doi: [10.1007/s10909-018-1982-4](https://doi.org/10.1007/s10909-018-1982-4)
- Cukierman, A., Ahmed, Z., Henderson, S., et al. 2020, Journal of Low Temperature Physics, 199, 858, doi: [10.1007/s10909-019-02296-2](https://doi.org/10.1007/s10909-019-02296-2)
- de Korte, P. A. J., Beyer, J., Deiker, S., et al. 2003, Review of Scientific Instruments, 74, 3807, doi: [10.1063/1.1593809](https://doi.org/10.1063/1.1593809)
- Dicker, S. R., Ade, P. A. R., Aguirre, J., et al. 2014, Journal of Low Temperature Physics, 176, 808, doi: [10.1007/s10909-013-1070-8](https://doi.org/10.1007/s10909-013-1070-8)
- Dobbs, M. A., Lueker, M., Aird, K. A., et al. 2012, Review of Scientific Instruments, 83, 073113, doi: [10.1063/1.4737629](https://doi.org/10.1063/1.4737629)
- Dober, B., Becker, D. T., Bennett, D. A., et al. 2017, Applied Physics Letters, 111, 243510, doi: [10.1063/1.5008527](https://doi.org/10.1063/1.5008527)
- Dober, B., Ahmed, Z., Arnold, K., et al. 2021, Applied Physics Letters, 118, 062601, doi: [10.1063/5.0033416](https://doi.org/10.1063/5.0033416)

- 395 Galitzki, N., Ali, A., Arnold, K. S., et al. 2018, in Society of
396 Photo-Optical Instrumentation Engineers (SPIE)
397 Conference Series, Vol. 10708, Millimeter, Submillimeter,
398 and Far-Infrared Detectors and Instrumentation for
399 Astronomy IX, ed. J. Zmuidzinas & J.-R. Gao, 1070804,
400 doi: [10.1117/12.2312985](https://doi.org/10.1117/12.2312985)
- 401 Gao, J., Daal, M., Martinis, J. M., et al. 2008, Applied
402 Physics Letters, 92, 212504, doi: [10.1063/1.2937855](https://doi.org/10.1063/1.2937855)
- 403 Gudmundsson, J. E., Gallardo, P. A., Puddu, R., et al.
404 2021, ApOpt, 60, 823, doi: [10.1364/AO.411533](https://doi.org/10.1364/AO.411533)
- 405 Healy, E., Ali, A. M., Arnold, K., et al. 2020, in Society of
406 Photo-Optical Instrumentation Engineers (SPIE)
407 Conference Series, Vol. 11453, Society of Photo-Optical
408 Instrumentation Engineers (SPIE) Conference Series,
409 1145317, doi: [10.1117/12.2561743](https://doi.org/10.1117/12.2561743)
- 410 Henderson, S. W., Allison, R., Austermann, J., et al. 2016,
411 Journal of Low Temperature Physics, 184, 772,
412 doi: [10.1007/s10909-016-1575-z](https://doi.org/10.1007/s10909-016-1575-z)
- 413 Henderson, S. W., Ahmed, Z., Austermann, J., et al. 2018,
414 in Society of Photo-Optical Instrumentation Engineers
415 (SPIE) Conference Series, Vol. 10708, Millimeter,
416 Submillimeter, and Far-Infrared Detectors and
417 Instrumentation for Astronomy IX, ed. J. Zmuidzinas &
418 J.-R. Gao, 1070819, doi: [10.1117/12.2314435](https://doi.org/10.1117/12.2314435)
- 419 Hill, C. A., Bruno, S. M. M., Simon, S. M., et al. 2018, in
420 Society of Photo-Optical Instrumentation Engineers
421 (SPIE) Conference Series, Vol. 10708, Millimeter,
422 Submillimeter, and Far-Infrared Detectors and
423 Instrumentation for Astronomy IX, ed. J. Zmuidzinas &
424 J.-R. Gao, 1070842, doi: [10.1117/12.2313916](https://doi.org/10.1117/12.2313916)
- 425 Irwin, K. D., & Hilton, G. C. 2005, Transition-Edge
426 Sensors, Vol. 99 (Springer), 63, doi: [10.1007/10933596_3](https://doi.org/10.1007/10933596_3)
- 427 Irwin, K. D., & Lehnert, K. W. 2004, Applied Physics
428 Letters, 85, 2107, doi: [10.1063/1.1791733](https://doi.org/10.1063/1.1791733)
- 429 Khalil, M. S., Stoutimore, M. J. A., Wellstood, F. C., &
430 Osborn, K. D. 2012, Journal of Applied Physics, 111,
431 054510, doi: [10.1063/1.3692073](https://doi.org/10.1063/1.3692073)
- 432 Li, Y., Arnold, K., Atkins, Z., et al. 2020, Journal of Low
433 Temperature Physics, 199, 985,
434 doi: [10.1007/s10909-020-02386-6](https://doi.org/10.1007/s10909-020-02386-6)
- 435 Mates, J. A. B. 2011, PhD thesis, University of Colorado at
436 Boulder
- 437 Mates, J. A. B., Hilton, G. C., Irwin, K. D., Vale, L. R., &
438 Lehnert, K. W. 2008, Applied Physics Letters, 92,
439 023514, doi: [10.1063/1.2803852](https://doi.org/10.1063/1.2803852)
- 440 Mather, J. C. 1982, ApOpt, 21, 1125,
441 doi: [10.1364/AO.21.001125](https://doi.org/10.1364/AO.21.001125)
- 442 Niemack, M. D. 2016, ApOpt, 55, 1686,
443 doi: [10.1364/AO.55.001686](https://doi.org/10.1364/AO.55.001686)
- 444 Rosenberg, D., Weber, S., Conway, D., et al. 2019, arXiv
445 e-prints, arXiv:1906.11146.
446 <https://arxiv.org/abs/1906.11146>
- 447 Sathyanarayana Rao, M., Silva-Feaver, M., Ali, A., et al.
448 2020, Journal of Low Temperature Physics, 199, 807,
449 doi: [10.1007/s10909-020-02429-y](https://doi.org/10.1007/s10909-020-02429-y)
- 450 Simon, S. M., Golec, J. E., Ali, A., et al. 2018, in Society of
451 Photo-Optical Instrumentation Engineers (SPIE)
452 Conference Series, Vol. 10708, Millimeter, Submillimeter,
453 and Far-Infrared Detectors and Instrumentation for
454 Astronomy IX, ed. J. Zmuidzinas & J.-R. Gao, 107084B,
455 doi: [10.1117/12.2313405](https://doi.org/10.1117/12.2313405)
- 456 Stevens, J. R., Cothard, N. F., Vavagiakis, E. M., et al.
457 2020, Journal of Low Temperature Physics, 199, 672,
458 doi: [10.1007/s10909-020-02375-9](https://doi.org/10.1007/s10909-020-02375-9)
- 459 Suzuki, A., Arnold, K., Edwards, J., et al. 2012, Journal of
460 Low Temperature Physics, 167, 852,
461 doi: [10.1007/s10909-012-0602-y](https://doi.org/10.1007/s10909-012-0602-y)
- 462 Suzuki, A., Ade, P., Akiba, Y., et al. 2016, Journal of Low
463 Temperature Physics, 184, 805,
464 doi: [10.1007/s10909-015-1425-4](https://doi.org/10.1007/s10909-015-1425-4)
- 465 Terry, H., Battaglia, N., Basu, K., et al. 2019, in Bulletin of
466 the American Astronomical Society, Vol. 51, 213.
467 <https://arxiv.org/abs/1909.02587>
- 468 The CMB-S4 Collaboration, :, Abazajian, K., et al. 2020,
469 arXiv e-prints, arXiv:2008.12619.
470 <https://arxiv.org/abs/2008.12619>
- 471 The Simons Observatory Collaboration, Ade, P., Aguirre,
472 J., et al. 2019, JCAP, 2019, 056,
473 doi: [10.1088/1475-7516/2019/02/056](https://doi.org/10.1088/1475-7516/2019/02/056)
- 474 Walker, S., Sierra, C., Austermann, J., et al. 2020, Journal
475 of Low Temperature Physics,
476 doi: <https://doi.org/10.1007/s10909-019-02316-1>
- 477 Xu, Z., Bhandarkar, T., Coppi, G., et al. 2020, in Society of
478 Photo-Optical Instrumentation Engineers (SPIE)
479 Conference Series, Vol. 11453, Society of Photo-Optical
480 Instrumentation Engineers (SPIE) Conference Series,
481 1145315, doi: [10.1117/12.2576151](https://doi.org/10.1117/12.2576151)
- 482 Xu, Z., Adachi, S., Ade, P., et al. 2021, Research Notes of
483 the American Astronomical Society, 5, 100,
484 doi: [10.3847/2515-5172/abf9ab](https://doi.org/10.3847/2515-5172/abf9ab)
- 485 Yoon, W., Adams, J. S., Bandler, S. R., et al. 2018, Journal
486 of Low Temperature Physics, 193, 258,
487 doi: [10.1007/s10909-018-1917-0](https://doi.org/10.1007/s10909-018-1917-0)
- 488 Zhu, N., Bhandarkar, T., Coppi, G., et al. 2021, arXiv
489 e-prints, arXiv:2103.02747.
490 <https://arxiv.org/abs/2103.02747>
- 491 Zmuidzinas, J. 2003, Appl. Opt., 42, 4989,
492 doi: [10.1364/AO.42.004989](https://doi.org/10.1364/AO.42.004989)